crystals

MDPI

Article

Atomic Characterization of Byproduct Nanoparticles on Cesium Lead Halide Nanocrystals Using High-Resolution Scanning Transmission Electron Microscopy

Mian Zhang, Hongbo Li, Qiang Jing, Zhenda Lu and Peng Wang *

National Laboratory of Solid State Microstructures, College of Engineering and Applied Sciences and Collaborative Innovation Center of Advanced Microstructures, Nanjing University, Nanjing 210093, China; mg1534034@smail.nju.edu.cn (M.Z.); lihongbo@nju.edu.cn (H.L.); jq05103113@163.com (Q.J.); luzhenda@nju.edu.cn (Z.L)

* Correspondence: wangpeng@nju.edu.cn

Received: 23 November 2017; Accepted: 20 December 2017; Published: 22 December 2017

Abstract: Recent microstructural studies on lead halide perovskite nanocrystals have consistently reported the coexistence of byproduct nanoparticles (NPs). However, the nature of these NPs and their formation mechanism are still a matter of debate. Herein, we have investigated the structure and compositions of the NPs located on colloidal cesium lead bromide nanocrystals ($CsPbBr_3$ NCs), mainly through aberration-corrected transmission electron microscopy and spectroscopy. Our results show that these NPs can be assigned to $PbBr_2$ and $CsPb_2Br_5$. The new $CsPb_2Br_5$ species are formed by reacting $CsPbBr_3$ NCs with the remaining $PbBr_2$ during the drying process. In addition, observation of the metallic Pb NPs are ascribed to the electron damage effect on $CsPbBr_3$ NCs during transmission electron microscopy imaging.

Keywords: lead halide perovskite materials; colloidal cesium lead halide nanocrystals; scanning transmission electron microscopy and spectroscopy

1. Introduction

Lead halide perovskite (LHP) materials have attracted significant attention in recent years, due to their promising applications in solar cells [1–5], light emitting diodes (LEDs) [6–9], lasers [10–13], and photo-detectors [14–17]. In the family of LHP materials, colloidal all-inorganic cesium lead halide ($CsPbX_3$, X = Cl, Br, and I) perovskite nanocrystals combine both high stability and superior high luminescent efficiency compared to their organic-inorganic counterparts [18,19]. With their colloidal properties, many works have concentrated on applying them to solution-processed devices such as display screens [20], lasers [12] and LEDs [8].

Recent studies have consistently reported the observation of nanoparticles (NPs) with high contrast to LHP nanocrystals ($CH_3NH_3PbBr_3$ [21] and $CsPbBr_3$ [22–26]) in transmission electron microscopy (TEM) images (i.e., the white dots in Figure 1). However, the structure, chemistry, and forming mechanism of these NPs are still unclear and under debate in these reports. Some reports indicate that these NPs are Pb metal, originating from either the precursor material $PbBr_2$ [26], or the electron damaged $CsPbBr_3$ lattices [23–25]. One report suggests that these NPs are $PbBr_2$ [21] and another report claims that these NPs are $CsPb_2Br_5$ [22].

Here, we demonstrate that these NPs exist as a mix of $PbBr_2$ and $CsPb_2Pb_5$ on the $CsPbBr_3$ nanocrystals (NCs). We propose a formation process of these NPs: (i) Excess reactant of $PbBr_2$ during the synthesis and, subsequently, incomplete purification of the $CsPbBr_3$ products, synergetically lead

to excess Pb^{2+} and Br^{-} dissolved in the $CsPbBr_3$ dispersion of nonpolar solvent. After the solvent evaporate from the carbon film, the $PbBr_2$ NPs quickly precipitate on the $CsPbBr_3$ NCs; (ii) The $PbBr_2$ NPs react with part of the $CsPbBr_3$ lattices to form the $CsPb_2Br_5$ NPs, still on the $CsPbBr_3$ NCs. Additional observation of the metallic Pb NPs are ascribed to the electron damage effect on $CsPbBr_3$ NCs during TEM imaging.

2. Results and Discussion

2.1. Morphology, Size, and Position

An overview of the NPs on the $CsPbBr_3$ NCs was first investigated using scanning TEM high-angle annular dark field (STEM-HAADF) images as shown in Figure 1. $CsPbBr_3$ NCs of about 15 nm with cubic and rectangular shapes are demonstrated. The NPs on the $CsPbBr_3$ NCs are of an average size of 2.72 ± 0.52 nm (inset of Figure 1a). These NPs have a tendency to locate near the edge of each $CsPbBr_3$ NC and a NP bridging itself between two $CsPbBr_3$ NCs has been even found (indicated with an arrow in Figure 1b), which suggests that these NPs do not locate inside the $CsPbBr_3$ lattice, but are attached to the surface of $CsPbBr_3$ NCs.

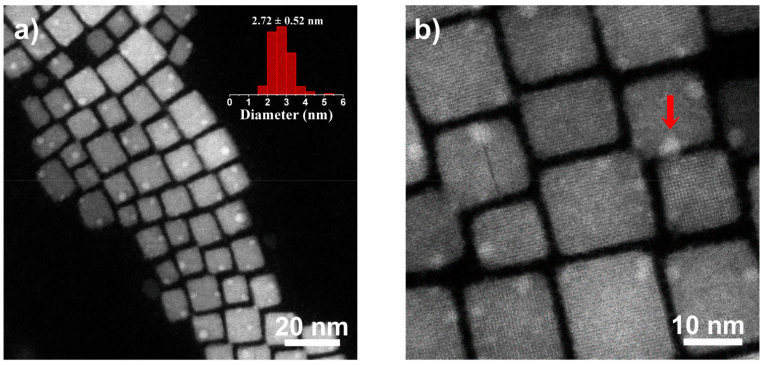

Figure 1. Overview STEM-HAADF images of the NPs on the $CsPbBr_3$ NCs at different magnifications. The inset of (**a**) shows the size distribution of over 300 NPs. The red arrow in (**b**) indicates a NP bridging itself between two $CsPbBr_3$ NCs.

2.2. Structure and Compositions

The structure of these NPs on the $CsPbBr_3$ NCs was first investigated by selected-area electron diffraction (SAED). As shown in Figure 2a, excluding the bright diffractive rings belonging to the $CsPbBr_3$ (100), (110), (200), (210), and (220) planes, additional spots indicated with arrows can be indexed as a $PbBr_2$ (121) plane and a $CsPb_2Br_5$ (114) plane. More SAED results are illustrated in Figure S1 to further verify the existence of both $PbBr_2$ NPs and $CsPb_2Br_5$ NPs. The identification of $PbBr_2$ and $CsPb_2Br_5$ is difficult to directly perform from their weak SAED patterns in the background of those from $CsPbBr_3$ NCs, as most low-index diffraction rings from $PbBr_2$ planes and $CsPb_2Br_5$ planes are overlapped with the much brighter ones from $CsPbBr_3$ planes (Table S1). Therefore, while much fewer diffraction spots corresponding to $PbBr_2$ and $CsPb_2Br_5$ are found in the SAED patterns compared with the large number of NPs observed in STEM-HAADF images, this is most likely due to the small size and poor crystallinity of the NPs expressing much weaker diffractive signals, largely covered by the signals from carbon films and $CsPbBr_3$ NCs. Later, the existence of the $PbBr_2$ and $CsPb_2Br_5$ NPs were further confirmed using high-resolution STEM-HAADF. Figure 2b shows a NP (about 3 nm in diameter) with an interplanar spacing of 2.55 Å, matching well with the $CsPb_2Br_5$ (312) plane (a PbBr textsubscript2 (230) plane is also possible). Note that other possible compounds, including Pb and CsBr, have all been taken into consideration and do not match with the above measurement results. Therefore, the NPs are preliminarily considered as a mix of $PbBr_2$ and $CsPb_2Br_5$.

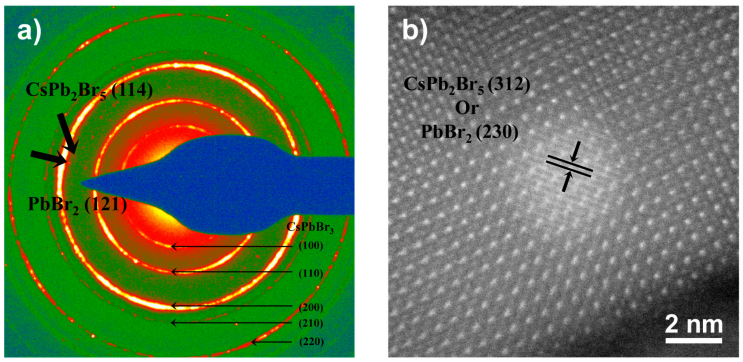

Figure 2. (**a**) SAED pattern of the NPs on the $CsPbBr_3$ NCs. Arrowed spots can be identified as $PbBr_2$ NPs and $CsPb_2Br_5$ NPs, excluding the main diffraction rings belonging to various $CsPbBr_3$ planes. (**b**) High-resolution STEM-HAADF image of a $CsPb_2Br_5$ NP (a $PbBr_2$ NP is also possible) formed on the $CsPbBr_3$ NC ($CsPbBr_3$, cubic phase, PDF#75-0412; $PbBr_2$, orthorhombic phase, PDF#31-0679; $CsPb_2Br_5$, tetragonal phase, PDF#25-0211).

In addition, metallic Pb NPs were also found on $CsPbBr_3$ NCs using high-resolution STEM-HAADF. Figure 3a,b shows the Pb (200) and Pb (020) atomic planes with a lattice spacing of 2.46 Å and an interfacial angle of 90°, oriented along a [001] zone axis. Since previous SAED results (Figure 2a) have implied no existence of metallic Pb, which contradicts the reported argument that metallic Pb NPs exist originally in the $CsPbBr_3$ dispersions [26], the Pb NPs found here at a high magnification (electron dose 1.9×10^5 $e^-/Å^2$) may, to a large extent, originate from the as-reported electron radiation effect on $CsPbBr_3$ lattice [23–25]. From Figure 3b, it is clear to see that the $CsPbBr_3$ lattices under the as-observed Pb NP were modified and damaged. Therefore, we propose that the metallic Pb NPs observed here may not be the extraneous NPs, like the $PbBr_2$ and $CsPb_2Br_5$ NPs, but rather a degradation product of $CsPbBr_3$ NCs from the focused electron beam during TEM imaging.

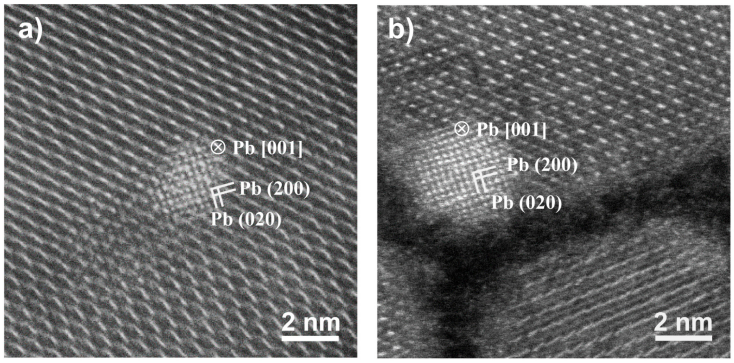

Figure 3. High-resolution STEM-HAADF images of the Pb NPs on the $CsPbBr_3$ NCs with [001] orientation (Pb, cubic phase, PDF#87-0663).

Furthermore, 2D energy dispersive spectroscopy (EDS) elemental mappings of several $CsPbBr_3$ NCs covered with the NPs (Figure 4a) was carried out to study the compositional information of the NPs. Due to the small size of the NPs and corresponding insufficient X-ray counts, the elemental maps (Figure 4a) have not shown strong variations of Cs, Pb, and Br in the position of the NPs. However, when we statistically calculated the atomic percentages of Cs (red), Pb (green), and Br (blue) from regions without the NPs (pure NC, i.e., indicated with a yellow circle in (a)) in comparison to that from regions with the NPs (NC+NP, i.e., indicated with a blue circle in (a)), as plotted in Figure 4b, it is evident to see that the NC+NP regions contain a lower atomic percentage of Br, more of Pb,

and a nearly constant percentage of Cs, compared to the pure NC regions. The increment of the Pb percentage in NC+NP regions was most likely caused by the existence of $PbBr_2$ and $CsPb_2Br_5$ NPs. However, a question may arise that, if the NPs consisted of $PbBr_2$ and $CsPb_2Br_5$, the Br percentage should, in theory, increase, which is unexpectedly inconsistent with the experimental data (blue curve) in Figure 4b.

In order to understand this discrepancy, we further directly compare the integrated EDS spectra of Cs, Pb, and Br taken from both NC+NP (a) and pure NC (b) regions, as shown in Figure 5. The two spectra were normalized with the peak of Cs as the only reactant of $PbBr_2$ was in excess during the synthesis. Regarding the signal of Br, it unexpectedly decreases for the NC+NP region compared to the pure NC region. In theory, the signal of Br should increase for the NC+NP region, if the additional NPs consisted of $PbBr_2$ and $CsPb_2Br_5$. However, by considering the inevitable electron-induced Br loss during EDS measurements [25], there is a high possibility that the existence of these NPs may lead to the structural instability of $CsPbBr_3$. As a result, the NC+NP region might have undergone an even more severe electron damage effect compared to the pure NC region, so that the electron-induced Br loss may surpass the theoretical Br increase coming from the extra existence of $PbBr_2$ and $CsPb_2Br_5$ NPs, causing the total Br intensity to decrease, as shown in Figure 5b and the Br percentage to unexpectedly decrease in Figure 4b. It can be concluded that the increase of the Pb percentage found in Figure 4b is not only due to the excess of $PbBr_2$ and $CsPb_2Br_5$ NPs, but also the Br loss induced by the strong electron damage effect in the NC+NP regions. It can also be understood that the atomic Br/Pb ratio (Figure 4c) being lower for the NC+NP regions, may be due to the interplay of the existence of $PbBr_2$ and $CsPb_2Br_5$ NPs whose Br/Pb ratio are lower than the stoichiometric one (3:1), and the Br loss induced by the strong electron damage effect in the NC+NP regions during EDS measurements. In addition, the increase of Pb intensity in the NC+NP region in Figure 5b further confirms that an excess Pb content exists in the NC+NP region, most likely in the forms of $PbBr_2$ and $CsPb_2Br_5$ NPs in addition to $CsPbBr_3$.

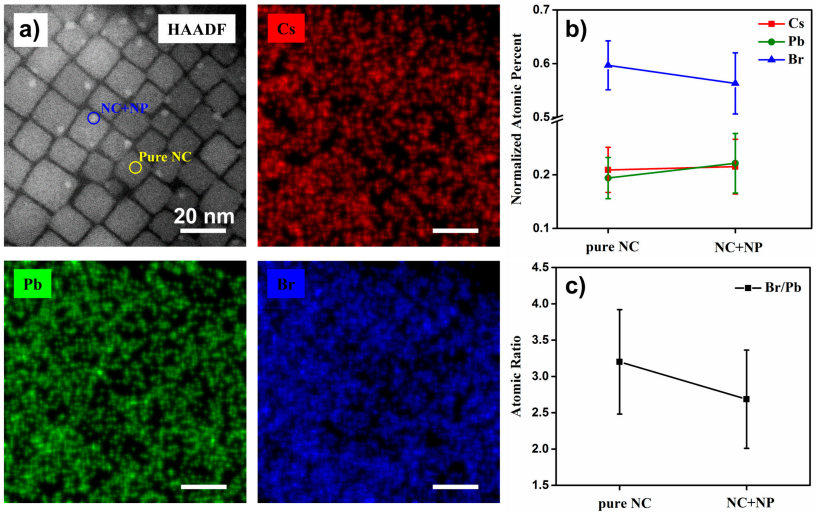

Figure 4. (**a**) STEM-EDS raw counts mappings of $CsPbBr_3$ NCs with the NPs. No strong variations of Cs, Pb, or Br are found in the position of the NPs. None of the auto-filter processing is applied here. (**b**) A plot of the calculated atomic percentages for Cs, Pb, and Br versus different regions (pure NC regions and NC+NP regions). We took an average of 10 quantified elemental atomic percentage results subtracted from 10 pure NC regions (i.e., indicated by a yellow circle in (**a**)). The error bar is the standard deviation. Similar calculations were applied to the NC+NP regions (i.e., indicated by a blue circle in (**a**)). (**c**) A plot of calculated atomic ratio of Br/Pb versus different regions (pure NC regions and NC+NP regions).

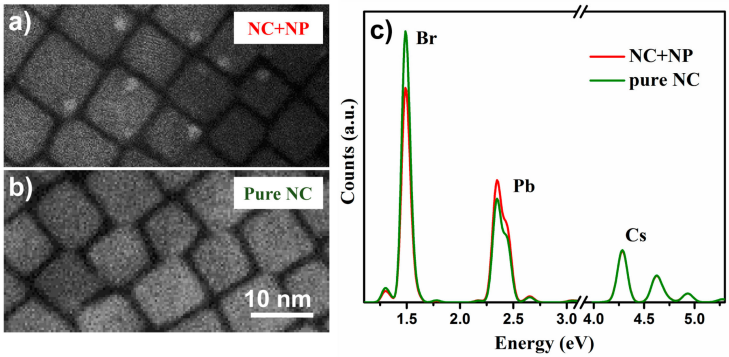

Figure 5. HAADF images of the NC+NP (**a**) and pure NC (**b**) regions. (**c**) Integrated EDS spectra acquired from NC+NP (—) and pure NC (—) regions as shown in (**a**) and (**b**), respectively.

2.3. Formation Mechanism

Here we suppose that the presence of $PbBr_2$ NPs can be ascribed to the excess $PbBr_2$ in the $CsPbBr_3$ dispersions. In our synthesis, molar ratio of reactant Cs:Pb:Br is controlled at about 1:3.3:6.6, which is similar to the most reported hot-injection procedures. Obviously, according to the stoichiometry ratio of $CsPbBr_3$ NCs, Cs species work as a limiting agent, and $PbBr_2$ is highly excessive in this reaction. In addition, incomplete purification of the $CsPbBr_3$ products during the following centrifugation step enables excess $PbBr_2$ to be left in the final $CsPbBr_3$ dispersions [27], existing as ion-complexes with oleic acid or oleylamine. When the drop of $CsPbBr_3$ dispersions on the ultrathin carbon film evaporates, the $CsPbBr_3$ NCs are spread out on the carbon film while the $PbBr_2$ NPs would precipitate on the carbon film or the upper surface of the NCs (Figure 6). This is consistent with the previous observation that the NPs are preferentially located at the corners and edges of the surface of $CsPbBr_3$ NCs. The chemical equilibrium reaction involved is as follows:

$$(C_{17}H_{33}COO)_2Pb + 2C_{18}H_{35}NH_2Br \rightarrow PbBr_2\downarrow + 2(C_{17}H_{33}COO)^-(C_{18}H_{35}NH_2)^+ \quad (1)$$

as the reaction shows, $PbBr_2$ would precipitate out, while oleate and oleylammonium form ion pairs. We note that if the above reaction was not complete, lead oleate and oleylammonium bromide may also precipitate out as separate species in the NPs. However, as it is difficult to directly characterize the structures of these organic non-crystalline materials through TEM imaging, the existence of lead oleate and oleylammonium bromide are not discussed here and are subject to future investigation.

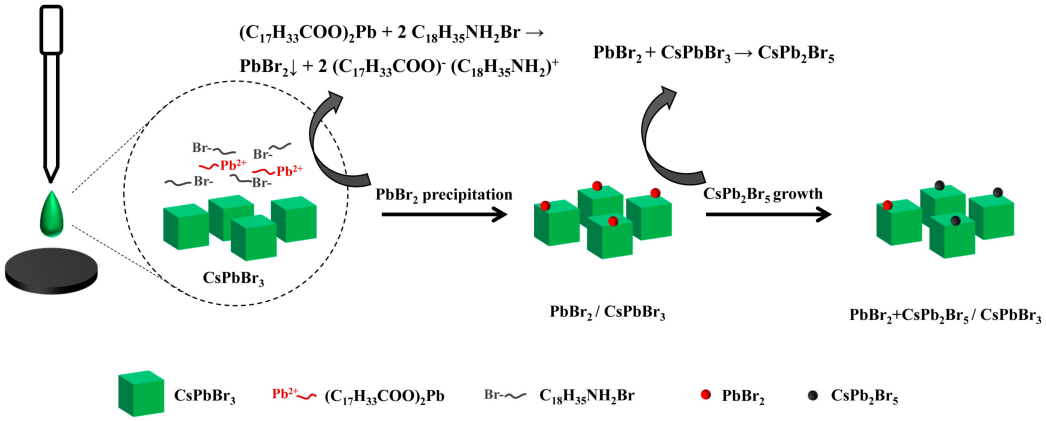

Figure 6. Schematic of the formation mechanism of the $PbBr_2$ NPs and the $CsPb_2Br_5$ NPs on $CsPbBr_3$ NCs.

Few reports have referred to the source of $CsPb_2Br_5$. One report demonstrated the existence of 10% $CsPb_2Br_5$ in the $CsPbBr_3$ solutions at room temperature [28]. Another report suggested that the excess $PbBr_2$ facilitates a structural transformation of small $CsPbBr_3$ nanocrystals in the precursor into $CsPb_2Br_5$ at a low temperature [22]. A recent report verified $CsPbBr_3$ nanocrystals can transfer to $CsPb_2Br_5$ nanosheets as the reaction time prolongs, clearly indicating this conversion (from $CsPbBr_3$ to $CsPb_2Br_5$) is thermodynamically favorable [29]. Therefore, we propose that the generation of $CsPb_2Br_5$ can be ascribed to the following process:

$$PbBr_2 + CsPbBr_3 \rightarrow CsPb_2Br_5 \quad (2)$$

The precipitated $PbBr_2$ NPs touch the $CsPbBr_3$ NC surface and tend to facilitate the generation of $CsPb_2Br_5$ NPs, as illustrated in Figure 6.

To confirm the contribution of excess $PbBr_2$ to the existence of the NPs, the remaining amount of $PbBr_2$ in the $CsPbBr_3$ dispersions were changed. Since directly changing the reactant amount may destroy the synthesis, we changed the purification times of the as-synthesized $CsPbBr_3$ products instead. Therefore, a comparison was made through TEM characterization between the following two samples: $CsPbBr_3$ NCs washed one time and $CsPbBr_3$ NCs washed three times. For the one-time wash sample, it is clear to see in Figure 7 that the NPs are evenly distributed both on the $CsPbBr_3$ NCs (a) and the carbon film (b), whereas for the sample washed three times with acetone, none of the NPs were found, neither on $CsPbBr_3$ NCs (c) or the carbon film (d). Moreover, the microstructure of the NPs on the carbon film was further confirmed by high-resolution TEM imaging and EDS elemental mapping. Figure 8a,b shows the high-resolution TEM images of two NPs on the carbon film. As shown in Figure 8a, the interplanar spacings of the NPs match well with the $PbBr_2$ (231) and $(42\bar{1})$ planes with an interfacial angle of 56°, oriented along a $[5\bar{6}8]$ axis. Additionally, in Figure 8b, the interplanar spacing of the NPs match well with the $PbBr_2$ (231) and $(\bar{2}12)$ planes with an interfacial angle of 74°, oriented along a $[5\bar{6}8]$ axis. Additionally, EDS measurements reveal that these NPs on the carbon film contain both Br and Pb, but lack Cs (See Figure S2 and Table S2). As a result, the unwashed NPs on the carbon film are verified to be $PbBr_2$. Therefore, it is confirmed that the excess reactant of $PbBr_2$ and incomplete purification contribute to the existence of the $PbBr_2$ NPs on both $CsPbBr_3$ NCs and carbon films.

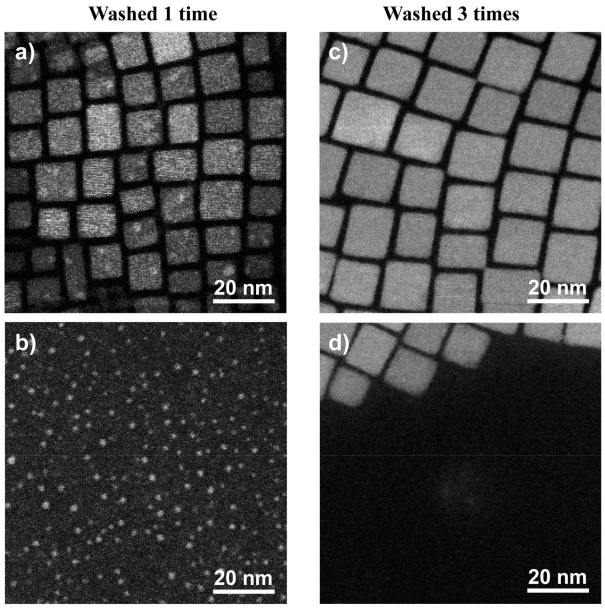

Figure 7. HAADF-STEM images of the distribution of the NPs on both $CsPbBr_3$ NCs and carbon films for the sample washed one time (**a**,**b**) and the sample washed three times (**c**,**d**), respectively.

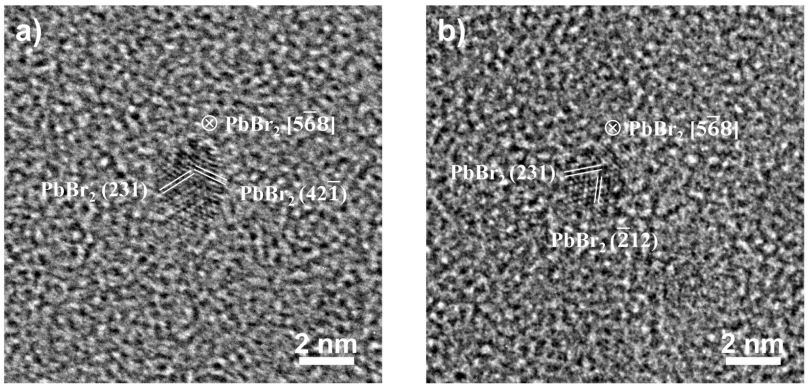

Figure 8. High-resolution TEM images of the $PbBr_2$ NPs found on carbon films along a [5$\bar{6}$8] axis.

As for the metallic Pb NPs, it was reported that the Pb NPs were formed in the $PbBr_2$ solution prior to injection of Cs salt [23], while another report investigated the effects of high energy electron radiation contributing to Br atoms desorption and Pb atoms crystallization [25]. Since previous SAEDs have indicated no Pb metals to exist, we assume that the original $CsPbBr_3$ dispersions have contained no Pb metals. Therefore, the observed Pb NPs by high-resolution HAADF-STEM might result from the electron damage effect on $CsPbBr_3$ NCs. Electron radiation (300 keV) induces desorption of Br atoms from the surface of the NCs and reduces Pb^{2+} cations to metallic Pb^0 atoms. Pb^0 atoms diffuse and aggregate into Pb NPs, oriented epitaxially on the $CsPbBr_3$ lattice.

3. Materials and Methods

3.1. Materials

Oleic acid (OA 90%), octadecene (ODE 90%), oleylamine (OAM 80–90%), cyclohexane, acetone, cesium carbonate (Cs_2CO_3 99.9%), and lead bromide ($PbBr_2$ 99.999%) were purchased from Aladdin (Shanghai, China). All chemicals were used as received without any further purification.

3.2. Synthesis of $CsPbBr_3$ Perovskite NCs

The $CsPbBr_3$ perovskite NCs adopted here were fabricated following a hot injection method [30]. For the synthesis of the $CsPbBr_3$, 0.1 g of $PbBr_2$ was added into a mixture of 7.5 mL ODE, 1.5 mL OAM, and 0.75 mL OA, and then heated to 120 °C for 30 min under vacuum. The temperature was then raised to 150 °C, followed by the rapid injection of 0.7 mL of Cs-oleate solution (0.407 g Cs_2CO_3 dissolved within 20 mL ODE and 1.5 mL OA). After several seconds, the solution was rapidly cooled by the water bath. The products were then washed via centrifugation with cyclohexane/acetone for one or three times. Finally the products were dispersed in cyclohexane forming long-term colloidally-stable dispersions.

3.3. Characterization of the NPs on the $CsPbBr_3$ NCs

TEM images, selected-area electron diffraction (SAED) patterns and scanning TEM high angle annular dark field (STEM-HAADF) images were acquired using a FEI Tecnai G2 F20 S-TWIN microscope, operated at an accelerating voltage of 200 kV. High-resolution TEM images, high-resolution STEM-HAADF images [31], and energy-dispersive spectroscopy (EDS) elemental mappings were acquired using a FEI Titan^3 G2 60-300 microscope, operated at an accelerating voltage of 300 kV, equipped with double aberration correctors [32] and Super-X EDS detectors [33]. The image pixel size in the high-resolution TEM and high-resolution STEM-HAADF images was calibrated using the ratio of the $CsPbBr_3$ lattice constant listed in the PDF card ($CsPbBr_3$, cubic phase, PDF#75-0412)

to the corresponding interplanar spacing pixels of the $CsPbBr_3$ NC measured in the image at the same magnification.

4. Conclusions

The TEM experiments presented here demonstrate that the byproduct NPs on $CsPbBr_3$ NCs is a mix of $PbBr_2$ and $CsPb_2Br_5$. We propose here that the excess reactant of $PbBr_2$ during the synthesis and, subsequently, the incomplete purification of the $CsPbBr_3$ products, synergetically led to the final excess precipitation of the $PbBr_2$ NPs on $CsPbBr_3$ NCs after solvent evaporation. The subsequent reaction between the $PbBr_2$ NPs and the $CsPbBr_3$ surface induce the formation of the $CsPb_2Br_5$ NPs. Moreover, the existence of these NPs may add to the structural instability of $CsPbBr_3$, so methods to remove these NPs are of great importance for maintaining their superior optical properties. Here, we propose that these byproduct NPs can be fully removed via washing $CsPbBr_3$ NCs three times with acetone. In addition, the metallic Pb NPs, which were not found in the original $CsPbBr_3$ dispersions, could be attributed to the electron damage of $CsPbBr_3$ NCs during TEM imaging. The above formation mechanism of the NPs on $CsPbBr_3$ NCs may also apply to other $CsPbX_3$ and hybrid lead halide perovskite nanocrystals.

Supplementary Materials: The following are available online at www.mdpi.com/2073-4352/8/1/2/s1; Figure S1: SAED patterns from two 0.48 μm^2 areas of the NPs on the $CsPbBr_3$ NCs; Figure S2: An integrated EDS spectrum acquired from a region with the NPs on a carbon film; Table S1: Interplanar spacings of $CsPbBr_3$, $PbBr_2$, and $CsPb_2Br_5$, respectively; Table S2: Atomic percentages of Cs, Pb, and Br for a region with the NPs on a carbon film.

Acknowledgments: This work was supported by the National Basic Research Program of China (grant no. 2015CB654901); the National Natural Science Foundation of China (11474147); the Natural Science Foundation of Jiangsu Province (grant no. BK20151383); the International Science and Technology Cooperation Program of China (2014DFE00200); and the Fundamental Research Funds for the Central Universities (no. 021314380077).

Author Contributions: Mian Zhang designed the experiments. Hongbo Li and Qiang Jing contributed sample materials. Mian Zhang performed the experiments and analyzed the dataset. Zhenda Lu and Peng Wang designed, supervised the project, and interpreted data.

Conflicts of Interest: The authors declare no conflict of interest.

References

1. Kojima, A.; Teshima, K.; Shirai, Y.; Miyasaka, T. Organometal halide perovskites as visible-light sensitizers for photovoltaic cells. *J. Am. Chem. Soc.* **2009**, *131*, 6050–6051. [CrossRef] [PubMed]
2. Lee, M.M.; Teuscher, J.; Miyasaka, T.; Murakami, T.N.; Snaith, H.J. Efficient hybrid solar cells based on meso-superstructured organometal halide perovskites. *Science* **2012**, *338*, 643–647. [CrossRef] [PubMed]
3. Liu, D.; Kelly, T.L. Perovskite solar cells with a planar heterojunction structure prepared using room-temperature solution processing techniques. *Nat. Photonics* **2014**, *8*, 133–138. [CrossRef]
4. Liu, M.; Johnston, M.B.; Snaith, H.J. Efficient planar heterojunction perovskite solar cells by vapour deposition. *Nature* **2013**, *501*, 395–398. [CrossRef] [PubMed]
5. Yang, W.S.; Noh, J.H.; Jeon, N.J.; Kim, Y.C.; Ryu, S.; Seo, J.; Seok, S.I. High-performance photovoltaic perovskite layers fabricated through intramolecular exchange. *Science* **2015**, *348*, 1234–1237. [CrossRef] [PubMed]
6. Cho, H.; Jeong, S.-H.; Park, M.-H.; Kim, Y.-H.; Wolf, C.; Lee, C.-L.; Heo, J.H.; Sadhanala, A.; Myoung, N.; Yoo, S. Overcoming the electroluminescence efficiency limitations of perovskite light-emitting diodes. *Science* **2015**, *350*, 1222–1225. [CrossRef] [PubMed]
7. Kim, Y.H.; Cho, H.; Heo, J.H.; Kim, T.S.; Myoung, N.; Lee, C.L.; Im, S.H.; Lee, T.W. Multicolored Organic/Inorganic Hybrid Perovskite Light-Emitting Diodes. *Adv. Mater.* **2015**, *27*, 1248–1254. [CrossRef] [PubMed]
8. Song, J.; Li, J.; Li, X.; Xu, L.; Dong, Y.; Zeng, H. Quantum Dot Light-Emitting Diodes Based on Inorganic Perovskite Cesium Lead Halides ($CsPbX_3$). *Adv. Mater.* **2015**, *27*, 7162–7167. [CrossRef] [PubMed]

9. Tan, Z.-K.; Moghaddam, R.S.; Lai, M.L.; Docampo, P.; Higler, R.; Deschler, F.; Price, M.; Sadhanala, A.; Pazos, L.M.; Credgington, D. Bright light-emitting diodes based on organometal halide perovskite. *Nat. Nanotechnol.* **2014**, *9*, 687–692. [CrossRef] [PubMed]
10. D'Innocenzo, V.; Srimath Kandada, A.R.; De Bastiani, M.; Gandini, M.; Petrozza, A. Tuning the light emission properties by band gap engineering in hybrid lead halide perovskite. *J. Am. Chem. Soc.* **2014**, *136*, 17730–17733. [CrossRef] [PubMed]
11. Deschler, F.; Price, M.; Pathak, S.; Klintberg, L.E.; Jarausch, D.-D.; Higler, R.; Huttner, S.; Leijtens, T.; Stranks, S.D.; Snaith, H.J. High photoluminescence efficiency and optically pumped lasing in solution-processed mixed halide perovskite semiconductors. *J. Phys. Chem. Lett.* **2014**, *5*, 1421–1426. [CrossRef] [PubMed]
12. Yakunin, S.; Protesescu, L.; Krieg, F.; Bodnarchuk, M.I.; Nedelcu, G.; Humer, M.; De Luca, G.; Fiebig, M.; Heiss, W.; Kovalenko, M.V. Low-threshold amplified spontaneous emission and lasing from colloidal nanocrystals of caesium lead halide perovskites. *Nat. Commun.* **2015**, *6*, 8056. [CrossRef] [PubMed]
13. Zhu, H.; Fu, Y.; Meng, F.; Wu, X.; Gong, Z.; Ding, Q.; Gustafsson, M.V.; Trinh, M.T.; Jin, S.; Zhu, X. Lead halide perovskite nanowire lasers with low lasing thresholds and high quality factors. *Nat. Mater.* **2015**, *14*, 636–642. [CrossRef] [PubMed]
14. Fang, Y.; Dong, Q.; Shao, Y.; Yuan, Y.; Huang, J. Highly narrowband perovskite single-crystal photodetectors enabled by surface-charge recombination. *Nat. Photonics* **2015**, *9*, 675–686. [CrossRef]
15. Hu, X.; Zhang, X.; Liang, L.; Bao, J.; Li, S.; Yang, W.; Xie, Y. High-performance flexible broadband photodetector based on organolead halide perovskite. *Adv. Funct. Mater.* **2014**, *24*, 7373–7380. [CrossRef]
16. Lee, Y.; Kwon, J.; Hwang, E.; Ra, C.H.; Yoo, W.J.; Ahn, J.H.; Park, J.H.; Cho, J.H. High-performance perovskite–graphene hybrid photodetector. *Adv. Mater.* **2015**, *27*, 41–46. [CrossRef] [PubMed]
17. Yakunin, S.; Sytnyk, M.; Kriegner, D.; Shrestha, S.; Richter, M.; Matt, G.J.; Azimi, H.; Brabec, C.J.; Stangl, J.; Kovalenko, M.V. Detection of X-ray photons by solution-processed lead halide perovskites. *Nat. Photonics* **2015**, *9*, 444–449. [CrossRef] [PubMed]
18. Protesescu, L.; Yakunin, S.; Bodnarchuk, M.I.; Krieg, F.; Caputo, R.; Hendon, C.H.; Yang, R.X.; Walsh, A.; Kovalenko, M.V. Nanocrystals of cesium lead halide perovskites ($CsPbX_3$, X = Cl, Br, and I): Novel optoelectronic materials showing bright emission with wide color gamut. *Nano Lett.* **2015**, *15*, 3692–3696. [CrossRef] [PubMed]
19. Wang, Y.; Li, X.; Song, J.; Xiao, L.; Zeng, H.; Sun, H. All-inorganic colloidal perovskite quantum dots: A new class of lasing materials with favorable characteristics. *Adv. Mater.* **2015**, *27*, 7101–7108. [CrossRef] [PubMed]
20. Yoon, H.C.; Kang, H.; Lee, S.; Oh, J.H.; Yang, H.; Do, Y.R. Study of perovskite QD down-converted LEDs and six-color white LEDs for future displays with excellent color performance. *ACS Appl. Mater. Interfaces* **2016**, *8*, 18189–18200. [CrossRef] [PubMed]
21. Sichert, J.A.; Tong, Y.; Mutz, N.; Vollmer, M.; Fischer, S.; Milowska, K.Z.; García Cortadella, R.; Nickel, B.; Cardenas-Daw, C.; Stolarczyk, J.K. Quantum size effect in organometal halide perovskite nanoplatelets. *Nano Lett.* **2015**, *15*, 6521–6527. [CrossRef] [PubMed]
22. Zhang, X.; Xu, B.; Zhang, J.; Gao, Y.; Zheng, Y.; Wang, K.; Sun, X.W. All-inorganic perovskite nanocrystals for high-efficiency light emitting diodes: Dual-phase cspbbr3-cspb2br5 composites. *Adv. Funct. Mater.* **2016**, *26*, 4595–4600. [CrossRef]
23. Van der, S.W.; Geuchies, J.J.; Altantzis, T.; Kh, V.D.B.; Meeldijk, J.D.; Van, A.S.; Bals, S.; Vanmaekelbergh, D.; De, M.D.C. Highly emissive divalent-ion-doped colloidal cspb1-xmxbr3 perovskite nanocrystals through cation exchange. *J. Am. Chem. Soc.* **2017**, *139*, 4087–4097. [CrossRef] [PubMed]
24. Tong, Y.; Bladt, E.; Aygüler, M.F.; Manzi, A.; Milowska, K.Z.; Hintermayr, V.A.; Docampo, P.; Bals, S.; Urban, A.S.; Polavarapu, L. Highly luminescent cesium lead halide perovskite nanocrystals with tunable composition and thickness by ultrasonication. *Angew. Chem.* **2016**, *55*, 13887–13892. [CrossRef] [PubMed]
25. Dang, Z.; Shamsi, J.; Palazon, F.; Imran, M.; Akkerman, Q.A.; Park, S.; Bertoni, G.; Prato, M.; Brescia, R.; Manna, L. In Situ Transmission Electron Microscopy Study of electron beam-induced transformations in colloidal cesiumlead halide perovskite nanocrystals. *Acs Nano* **2017**, *11*, 2124–2132. [CrossRef] [PubMed]
26. Udayabhaskararao, T.; Kazes, M.; Houben, L.; Lin, H.; Oron, D. Nucleation, growth, and structural transformations of perovskite nanocrystals. *Chem. Mater.* **2017**, *29*, 1302–1308. [CrossRef]
27. Gonzalez-Carrero, S.; Galian, R.E.; Pérez-Prieto, J. Maximizing the emissive properties of $CH_3NH_3PbBr_3$ perovskite nanoparticles. *J. Mater. Chem. A* **2015**, *3*, 9187–9193. [CrossRef]

28. Rodová, M.; Brožek, J.; Knížek, K.; Nitsch, K. Phase transitions in ternary caesium lead bromide. *J. Therm. Anal. Calorim.* **2003**, *71*, 667–673. [CrossRef]
29. Li, G.; Wang, H.; Zhu, Z.; Chang, Y.; Zhang, T.; Song, Z.; Jiang, Y. Shape and phase evolution from $CsPbBr_3$ perovskite nanocubes to tetragonal $CsPb_2Br_5$ nanosheets with an indirect bandgap. *Chem. Commun.* **2016**, *52*, 11296–11299. [CrossRef] [PubMed]
30. Talapin, D.V.; Lee, J.-S.; Kovalenko, M.V.; Shevchenko, E.V. Prospects of colloidal nanocrystals for electronic and optoelectronic applications. *Chem. Rev.* **2009**, *110*, 389–458. [CrossRef] [PubMed]
31. Muller, D.A. Structure and bonding at the atomic scale by scanning transmission electron microscopy. *Nat. Mater.* **2009**, *8*, 263–270. [CrossRef] [PubMed]
32. Hutchison, J.L.; Titchmarsh, J.M.; Cockayne, D.J.; Doole, R.C.; Hetherington, C.J.; Kirkland, A.I.; Sawada, H. A versatile double aberration-corrected, energy filtered HREM/STEM for materials science. *Ultramicroscopy* **2005**, *103*, 7–15. [CrossRef] [PubMed]
33. Allen, L.J.; D'Alfonso, A.J.; Freitag, B.; Klenov, D.O. Chemical mapping at atomic resolution using energy-dispersive X-ray spectroscopy. *MRS Bull.* **2012**, *37*, 47–52. [CrossRef]